Nano Research

ISSN 1998-0124 CN 11-5974/O4
https://doi.org/10.26599/NR.2026.94908974

Research Article

Dual-anion synergistic protection of NiFe layered double hydroxide for durable alkaline seawater oxidation

Zhengwei Cai[1,§], Zixiao Li[2,§], Yang Li[3,§], Wencong Xu[2], Mingyu Liu[2], Dongrui Li[2], Shengjun Sun[2], Mohamed S. Hamdy[4], Asmaa Farouk[4], Xiaodong Zhang[1](✉), Qiang Yu[1](✉), Xuping Sun[2,5](✉)

[1] Laoshan Laboratory, Qingdao 266237, China

[2] College of Chemistry, Chemical Engineering and Materials Science, Shandong Normal University, Jinan 250014, China

[3] Division of Gastrointestinal Surgery Ward, Department of Generl Surgery, West China Hospital, Sichuan University, Chengdu 610041, China

[4] Central Labs & Research Center for Advanced Materials Science (RCAMS), King Khalid University, Abha 61413, Saudi Arabia

[5] Center for High Altitude Medicine, West China Hospital, Sichuan University, Chengdu 610041, China

[§] Zhengwei Cai, Zixiao Li, and Li Yang contributed equally to this work.

Nano Res., **Just Accepted Manuscript** • https://doi.org/10.26599/NR.2026.94908974

https://www.sciopen.com/journal/1998-0124 on Jun. 26, 2026

Just Accepted

Dual-anion synergistic protection of NiFe layered double hydroxide for durable alkaline seawater oxidation

Zhengwei Cai[1§], Zixiao Li[2§], Yang Li[3§], Wencong Xu[2], Mingyu Liu[2], Dongrui Li[2], Shengjun Sun[2], Mohamed S. Hamdy[4], Asmaa Farouk[4], Xiaodong Zhang[1*], Qiang Yu[1*], and Xuping Sun[2,5*]

1. Laoshan Laboratory, China
2. Shandong Normal University, China
3. West China Hospital, Sichuan University, China
4. King Khalid University, Saudi Arabia
5. West China Hospital, Sichuan University, China

§ Zhengwei Cai, Zixiao Li, and Yang Li contributed equally to this work.

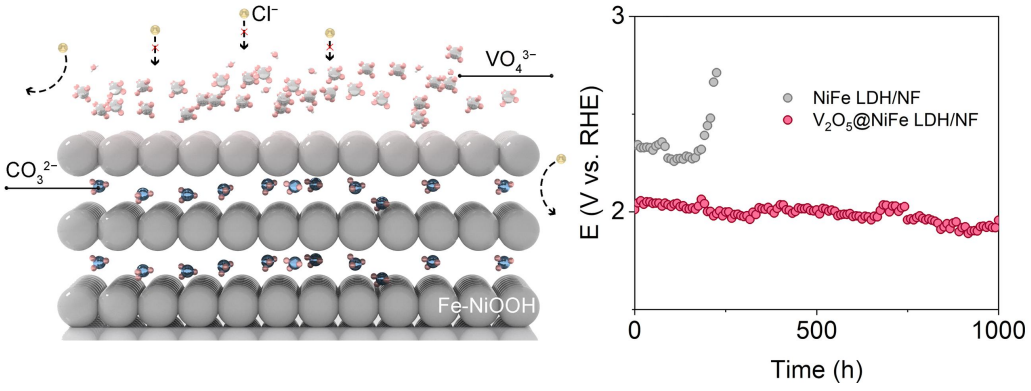

Enabled by the cooperative protection of surface VO_4^{3-} and interlayer CO_3^{2-}, V_2O_5@NiFe LDH/NF achieves an overpotential of only 370 mV at 1000 mA cm^{-2} and sustains continuous operation for 1000 h under industrial-level current density. Moreover, the anion-exchange membrane electrolyzer employing V_2O_5@NiFe LDH/NF as the anode and Pt/C/NF as the cathode delivers 500 mA cm^{-2} at a low cell voltage of 2.02 V and remains stable for 1000 h.

Nano Research

ISSN 1998-0124 CN 11-5974/O4
https://doi.org/10.26599/NR.2026.94908974

Research Article

Dual-anion synergistic protection of NiFe layered double hydroxide for durable alkaline seawater oxidation

Zhengwei Cai[1§], Zixiao Li[2§], Yang Li[3§], Wencong Xu[2], Mingyu Liu[2], Dongrui Li[2], Shengjun Sun[2], Mohamed S. Hamdy[4], Asmaa Farouk[4], Xiaodong Zhang[1](✉), Qiang Yu[1](✉), and Xuping Sun[2,5](✉)

[1] *Laoshan Laboratory, Qingdao 266237, China*

[2] *College of Chemistry, Chemical Engineering and Materials Science, Shandong Normal University, Jinan 250014, China*

[3] *Division of Gastrointestinal Surgery Ward, Department of Generl Surgery, West China Hospital, Sichuan University, Chengdu 610041, China*

[4] *Central Labs & Research Center for Advanced Materials Science (RCAMS), King Khalid University, Abha 61413, Saudi Arabia*

[5] *Center for High Altitude Medicine, West China Hospital, Sichuan University, Chengdu 610041, China*

[§] Zhengwei Cai, Zixiao Li, and Li Yang contributed equally to this work.

Received: 27 May 2026 / **Revised:** 19 June 2026 / **Accepted:** 26 June 2026

ABSTRACT

Seawater electrolysis is promising for green hydrogen production but suffers from chloride-induced anodic corrosion. Herein, a dual-anion synergistic protection strategy is proposed for durable alkaline seawater oxidation over V_2O_5 nanolayer coated NiFe layered double hydroxide nanosheets on Ni foam (V_2O_5@NiFe LDH/NF). During seawater oxidation process, the surface V_2O_5 component is reconstructed into adsorbed VO_4^{3-} species as an anion-enriched protective interface capable of electrostatically repelling Cl^- and mitigating chloride attack. In parallel, the interlayer CO_3^{2-} confined within NiFe LDH acts as an internal anionic barrier, suppressing Cl^- penetration into the LDH galleries and inhibiting its adsorption on catalytically active sites. The cooperative action of external VO_4^{3-} protection and internal CO_3^{2-} shielding endows V_2O_5@NiFe LDH/NF with robust catalytic activity and exceptional durability, delivering an overpotential of 370 mV at 1000 mA cm^{-2} and maintaining stable operation for 1000 h under industrial-level current density. Furthermore, an anion-exchange membrane electrolyzer assembled with V_2O_5@NiFe LDH/NF as the anode and Pt/C/NF as the cathode requires only 2.02 V to achieve 500 mA cm^{-2} and operates continuously for 1000 h. This study provides a rational dual-anion interfacial engineering strategy for developing durable electrodes under harsh chloride-containing environments.

KEYWORDS

seawater electrolysis, dual-anion protection, chloride corrosion resistance, long-term stability

1 Introduction

The escalating global energy demand and the increasing pressure for carbon neutrality have intensified the need for a fundamental transition from fossil-fuel-dominated energy systems to sustainable energy infrastructures, and hydrogen (H_2) is a zero-emission energy carrier alternative for realizing the global carbon neutrality target [1–3]. H_2 is also proven as a potent therapeutic antioxidant for medical applications [4,5]. Water electrolysis is commercially utilized for large-scale production of high-purity green H_2 [6–14], but freshwater suffers from limited supply and only accounts for only 2.5% of the Earth's total water resources [15,16]. Direct seawater electrolysis has thus attracted increasing attention as a sustainable route for H_2 production, since it can make use of an abundant and geographically accessible water resource while reducing dependence on freshwater supplies [17–27]. Nevertheless, the chloride-rich nature of seawater remains a major challenge to durable electrolysis. During seawater oxidation, chloride ion (Cl^-) can aggressively corrode oxygen evolution reaction (OER) electrocatalysts and simultaneously promote parasitic chlorine-involved reactions, thereby accelerating catalyst degradation, shortening the service lifetime of the electrolyzer, and increasing the energy input required for long-term device operation. Given that sustaining structural and catalytic integrity at high densities (j) remains a critical challenge for durable seawater electrolysis, developing highly active and chlorine-resistant OER anodes is essential for advancing seawater electrolysis toward practical application.

Layered double hydroxides (LDHs) have been widely recognized as superb OER catalysts [28,29] and recent years have witnessed the rapid advancements in developing NiFe LDHs-based ASO catalysts [18,19,30–36]. Creating anion-enriched protective interfaces is proven as an effective strategy to mitigate Cl^- adsorption via strong electrostatic repulsion. However, the protective efficacy of a single anion-mediated interfacial layer is frequently weakened by its limited compactness and spatially heterogeneous surface distribution at industrial-grade j. A more robust design should integrate multiple anionic protection modes into one catalyst architecture, enabling both external interfacial Cl^- repulsion and internal structural shielding. Such a dual-anion

Address correspondence to Xiaodong Zhang, xdzhang_qnlm@163.com; Qiang Yu, qyu1@lsnl.cn; Xuping Sun, xpsun@uestc.edu.cn.

synergistic protection system is expected to construct a dense and continuous anion-rich interface, regulate competitive ion adsorption, and isolate active sites from corrosive chloride species, thereby improving both structural stability and catalytic durability.

Herein, we report an amorphous V_2O_5-modified NiFe LDH electrode supported on Ni foam (V_2O_5@NiFe LDH/NF), prepared through a combined hydrothermal and electrodeposition strategy. The V_2O_5@NiFe LDH/NF functions as a highly active and durable anode for ASO. During ASO, the surface V_2O_5 component undergoes in situ reconstruction into adsorbed VO_4^{3-} species, which synergize with interlayer CO_3^{2-} anions in NiFe LDH to construct a dual-anion protective interface. The high-charge-density VO_4^{3-} species create a strongly anionic surface environment to repel Cl^- migration and inhibit metal–chloride coordination, while the confined interlayer CO_3^{2-} anions act as an internal barrier to block Cl^- penetration into the inner active regions, thereby protecting metal active sites from chloride-induced corrosion. Benefiting from this external VO_4^{3-} protection and internal CO_3^{2-} shielding, V_2O_5@NiFe LDH/NF exhibits an overpotential (η) of only 370 mV at 1000 mA cm^{-2}, together with stable operation for 1000 h under industrial-level *j*. Moreover, when employed as the anode in an anion-exchange membrane (AEM) electrolyzer paired with Pt/C/NF as the cathode, the device delivers 500 mA cm^{-2} at a low cell voltage of 2.02 V and maintains continuous operation for 1000 h. This work demonstrates a dual-anion interfacial engineering strategy for developing corrosion-resistant OER electrodes toward durable ASO at high *j*.

2 Experimental

2.1 Materials

Analytical-grade chemicals were used throughout the experiments without further purification. Nickel nitrate hexahydrate ($Ni(NO_3)_2·6H_2O$), iron nitrate nonahydrate ($Fe(NO_3)_3·9H_2O$), ammonium fluoride (NH_4F), urea ($CO(NH_2)_2$), potassium hydroxide (KOH), sodium carbonate (Na_2CO_3), tetramethylammonium hydroxide (TMAOH), anhydrous ethanol (C_2H_5OH), vanadium pentoxide (V_2O_5), and N,N-diethyl-p-phenylenediamine (DPD) were obtained from Beijing Chemical Reagent Co., Ltd. (Beijing, China). Ruthenium dioxide (RuO_2) and 5 wt.% Nafion solution were supplied by Aladdin Ltd. (Shanghai, China), while Ni foam (NF) was provided by Xingtai Qingyuan Metal Materials Co., Ltd. Natural seawater used in this study was collected from the coastal area of Qingdao, Shandong Province, China.

2.2 Sample preparation procedure

2.2.1 Preparation of NiFe LDH/NF

A piece of NF (2.0×3.0 cm^2) as first cleaned by sequential ultrasonication in 3 M HCl, anhydrous ethanol, and ultrapure water for at least 10 min each, in order to remove surface oxides and adsorbed impurities. The cleaned NF was subsequently placed vertically in a Teflon-lined stainless-steel autoclave containing 50 mL of precursor solution. The aqueous precursor was prepared by dissolving 1 mM $Ni(NO_3)_2·6H_2O$, 1 mM $Fe(NO_3)_3·9H_2O$, 4 mM NH_4F, and 10 mM $CO(NH_2)_2$ in ultrapure water, with the Ni/Fe molar ratio fixed at 1:1. The autoclave was sealed and heated at 120 °C for 6 h to allow hydrothermal growth. After cooling naturally to room temperature, the obtained sample was removed, thoroughly washed with ultrapure water and anhydrous ethanol, and then dried at 60 °C for 12 h.

2.2.2 Preparation of V_2O_5@NiFe LDH/NF

Electrodeposition was performed in a standard three-electrode configuration using NiFe LDH/NF as the working electrode, Ag/AgCl as the reference electrode, and a Pt plate as the counter electrode. NiFe LDH/NF electrode was immersed in 0.25 M $VOSO_4$ electrolyte and polarized at 1.5 V versus Ag/AgCl for 10 min to introduce the V-containing surface layer. The resulting electrode was subsequently collected, thoroughly washed with ultrapure water and ethanol, and dried at 60 °C for 24 h.

2.2.3 Preparation of RuO_2/NF and Pt/C/NF

5 mg of RuO_2 or Pt/C catalyst was added into the mixed solution consisting of 30 μL Nafion, 485 μL anhydrous ethanol and 485 μL ultrapure water. After 30 min ultrasonic dispersion, catalyst ink of 5 mg mL^{-1} was obtained. Then 300 μL ink was evenly coated on precleaned NF (0.5×0.5 cm^2) with the catalyst loading controlled at 6 mg cm^{-2}.

2.2.4 Preparation of alkaline seawater

First, 6.8 g of Na_2CO_3 was added to 1 L of natural seawater under stirring. After standing for half a day, the mixture was pumped. Subsequently, 1 M KOH was added to 1 L of the filtrate, and after standing overnight, the solution was centrifuged to obtain alkaline seawater.

2.3 Characterizations

The morphology and microstructure of the prepared samples were characterized using field-emission scanning electron microscopy (SEM, SU8010), transmission electron microscopy (TEM, Zeiss Libra 200FE), and high-resolution transmission electron microscopy (HRTEM, FEI Tecnai G2 F20). The crystalline phases were examined by X-ray diffraction (XRD, XRD-7000) with Cu Kα radiation operated at 40 kV and 30 mA, while the surface elemental composition and chemical states were analyzed by X-ray photoelectron spectroscopy (XPS, ESCALAB250). UV–vis absorption spectra were collected on a Shimadzu UV-2700 spectrophotometer. Raman spectra were recorded using a LabRAM HR Evolution confocal Raman microscope with a 532 nm excitation laser. Isotope-labeling measurements were carried out on an in situ differential electrochemical mass spectrometer (DEMS, QAS100).

2.4 Electrochemical tests

All electrochemistry measurements were performed with a CHI660E electrochemical workstation in a standard three-electrode system. The as-prepared V_2O_5@NiFe LDH/NF electrode was directly used as the working electrode, with a carbon rod as the counter electrode and Hg/HgO as the reference electrode. All measured potentials were calibrated to the reversible hydrogen electrode (RHE) according to E (RHE) = E (Hg/HgO) + 0.059 × pH + 0.197 V. The electrolyte used for the measurements was alkaline seawater containing 1 M KOH. The reported current densities were normalized to the geometric surface area of the

electrode, namely 0.25 cm^2.

2.5 Determination of active chlorine

UV-vis spectrophotometer was utilized to determine the concentration of active chlorine in the electrolyte through the DPD colorimetric method. After electrolysis at 1000 mA cm^{-2} in 1 M KOH + seawater, DPD was added to the electrolyte, causing a pink coloration. UV-vis absorption spectrometry at 550 nm was used to analyze different active chlorine concentrations.

2.6 Computational details

All DFT calculations were carried out with the DMol[3] code. The generalized gradient approximation with the Perdew-Burke-Ernzerh of exchange-correlation functional was used throughout the calculations. Atomic orbitals were expanded using a double numerical plus polarization basis set. The Grimme DFT-D correction was applied to describe dispersion interactions. Geometry optimizations were performed until the total energy, maximum force, and maximum displacement were converged to 1.0×10^{-5} Ha, 0.002 Ha $Å^{-1}$, and 0.005 Å, respectively. The convergence criterion for the SCF procedure was set to 1.0×10^{-6} Ha.

3 Results and discussion

As shown in the XRD patterns (Figure 1a), both NiFe LDH/NF and V_2O_5@NiFe LDH/NF display three intense diffraction peaks at 2θ values of approximately 44.5°, 51.8°, and 76.4°, which can be indexed to the (111), (200), and (220) planes of metallic Ni from the NF substrate (PDF#04-0850). In addition to these intense substrate signals, weak and broadened reflections appearing in the low-angle region can be assigned to the NiFe LDH phase, indicating the successful formation of a low-crystallinity layered hydroxide structure on the conductive NF framework. No obvious diffraction peaks corresponding to crystalline V_2O_5 are observed for V_2O_5@NiFe LDH/NF, which is likely due to the amorphous nature and/or relatively low loading amount of the deposited V_2O_5 layer. Raman spectroscopy was further performed to probe the local structural features of the catalysts. Inductively coupled plasma optical emission spectroscopy (ICP-OES) analysis confirms the successful V loading on the NiFe LDH surface and demonstrates the good reproducibility of the electrodeposition process for preparing V_2O_5@NiFe LDH/NF (Table S1). As displayed in Figure 1b, NiFe LDH/NF shows typical LDH-related vibrational bands at 457 and 537 cm^{-1}, while the band located near 1060 cm^{-1} is associated with interlayer CO_3^{2-} species. After V_2O_5 modification, the characteristic Raman signals of NiFe LDH are largely retained, suggesting that the LDH framework remains stable during the electrodeposition process. Notably, a new band at 698 cm^{-1} appears in V_2O_5@NiFe LDH/NF, which is attributed to the bridging V–O–V vibration of V_2O_5 [37], confirming the successful incorporation of V_2O_5 onto the NiFe LDH surface. The morphology of the catalysts was then examined by SEM. As shown in Figures 1c and 1d, V_2O_5@NiFe LDH/NF presents a stacked two-dimensional nanosheet architecture uniformly grown on the three-dimensional NF skeleton, forming an open porous network that is favorable for exposing abundant active sites and facilitating electrolyte penetration. NiFe LDH/NF displays a similar nanosheet morphology, as shown in Figure S1, indicating that V_2O_5 electrodeposition does not destroy the original LDH architecture. TEM, HRTEM, and EDS elemental mapping were further employed to reveal the nanoscale structure and elemental distribution of V_2O_5@NiFe LDH/NF. Low-magnification TEM image in Figure 1e shows well-defined ultrathin nanosheets with transparent edges and obvious wrinkles, consistent with the layered nature of NiFe LDH. As shown in Figure 1f, distinct lattice fringes with an interplanar spacing of 0.232 nm are observed in selected regions, corresponding to the (015) plane of NiFe LDH, whereas the outer regions exhibit blurred lattice fringes and disordered contrast, implying the formation of an amorphous V_2O_5 coating on the crystalline LDH nanosheets. Furthermore, HAADF-STEM coupled with EDS mapping in Figure 1g reveals the homogeneous distribution of Ni, Fe, V, and O throughout the nanosheets, without obvious elemental aggregation or phase separation. These results collectively demonstrate the successful construction of an amorphous V_2O_5-modified NiFe LDH heterostructure on NF.

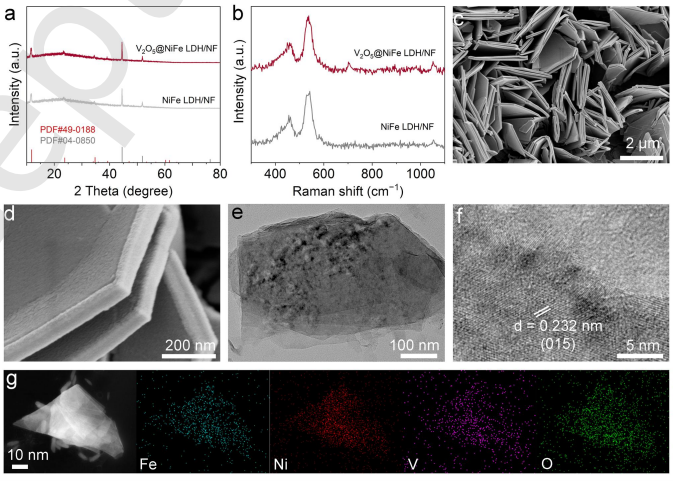

Figure 1 (a) XRD pattern of V_2O_5@NiFe LDH/NF and NiFe LDH/NF. (b) Raman spectra of V_2O_5@NiFe LDH/NF and NiFe LDH/NF. (c) Low- and (d) high-magnification SEM images of V_2O_5@NiFe LDH/NF. (e) TEM and (f) HRTEM images of V_2O_5@NiFe LDH. (g) Energy dispersive spectroscopy elemental mapping images for V_2O_5@NiFe LDH.

High-resolution XPS spectra of NiFe LDH and V_2O_5@NiFe LDH are compared to clarify the influence of introduced V_2O_5 on the surface electronic structure of the as-prepared materials. XPS survey spectrum verifies the simultaneous existence of characteristic signals corresponding to Ni, Fe, O, V, and C in V_2O_5@NiFe LDH (Figure S2a). In addition, clear V characteristic peaks appear in the V 2p spectra (Figure S2b). The peaks at around 517-518 eV and 524-525 eV are assigned to V $2p_{3/2}$ and V $2p_{1/2}$, respectively. This confirms the successful introduction of V species in the composite. The chemical state of V mainly exists in high-valence form, which matches the composition characteristics of V_2O_5 [38,39]. Figure S2c presents the Ni 2p high-resolution spectra. The peaks near 855 eV and 873 eV of NiFe LDH are assigned to Ni $2p_{3/2}$ and Ni $2p_{1/2}$, respectively [40]. Compared with pristine NiFe LDH, the Ni 2p peaks in

V_2O_5@NiFe LDH shift positively by 0.1-0.2 eV toward higher binding energy. It reveals decreased electron density around Ni sites and moderate electron deficiency at Ni centers. This result demonstrates that distinct electron redistribution occurs at the heterointerface after constructing V_2O_5@NiFe LDH. Electrons tend to transfer from NiFe LDH to V–O species, which modulates the local coordination environment and electronic state distribution of Ni active sites. Figure S2d shows the Fe 2p high-resolution spectra. The main Fe 2p peaks in V_2O_5@NiFe LDH also shift slightly positively compared with NiFe LDH. The Fe $2p_{3/2}$ and Fe $2p_{1/2}$ peaks exhibit shifts of approximately 0.05 eV and 0.1 eV respectively. This trend is consistent with the Ni 2p results. It further proves that V_2O_5 loading is not a simple physical mixture. Instead, it induces electronic structure modulation of Ni and Fe sites at the heterostructure interfaces. The appearance of V 2p signals confirms the successful construction of V_2O_5 on NiFe LDH at the elemental level. Combined with the binding energy shifts of Ni and Fe, it further demonstrates the formation of stable electronically coupled interfaces in the composite.

The natural seawater is collected from Huangdao district, Qingdao, China, and pretreated by Na_2CO_3 precipitation, KOH alkalization, and centrifugation to effectively remove Ca^{2+}/Mg^{2+} species (Table S2). Figure 2a compare the OER polarization curves of different electrodes in alkaline seawater electrolyte. V_2O_5@NiFe LDH/NF exhibits a markedly lower potential than NiFe LDH/NF, RuO_2/NF, and bare NF at the same j, requiring an η of only 370 mV to reach 1000 mA cm^{-2}, indicative of its superior electrocatalytic activity. The LSV curves without iR compensation further show that V_2O_5@NiFe LDH/NF requires a lower potential than NiFe LDH/NF at the same j, confirming its superior OER activity (Figure S3). The corresponding Tafel plots in Figure 2b were further analyzed to evaluate the reaction kinetics. V_2O_5@NiFe LDH/NF delivers a small Tafel slope of 33.91 mV dec^{-1}, which is lower than those of NiFe LDH/NF (40.49 mV dec^{-1}), RuO_2/NF (63.30 mV dec^{-1}), and bare NF (128.89 mV dec^{-1}), suggesting that V_2O_5 modification effectively accelerates the OER kinetics and enables a rapid current response with increasing η. Electrochemical impedance

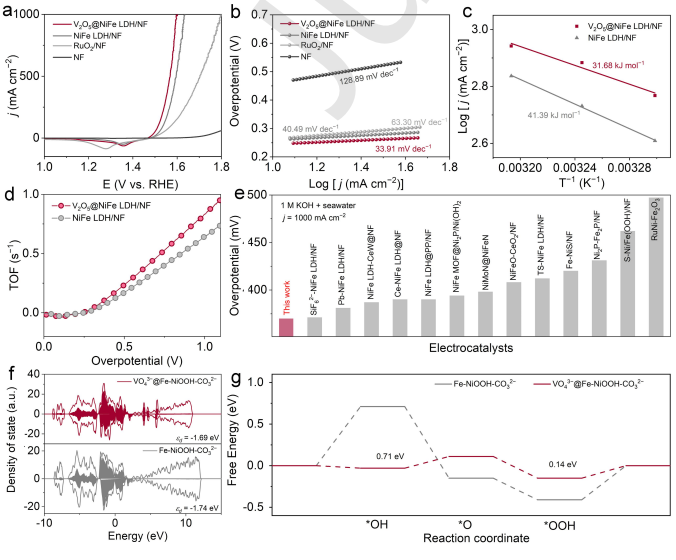

Figure 2 (a) LSV curves and (b) corresponding Tafel plots of different electrocatalysts in 1 M KOH + seawater. (c) Comparison of Arrhenius plots for V_2O_5@NiFe LDH/NF and NiFe LDH/NF. (d) TOF plots of V_2O_5@NiFe LDH/NF and NiFe LDH/NF. (e) Comparison of the η for V_2O_5@NiFe LDH/NF and other reported seawater OER electrocatalysts. (f) DOS plots of Fe-NiOOH-CO_3^{2-} and VO_4^{3-}@Fe-NiOOH-CO_3^{2-} (the shaded area represents the density of states corresponding to Ni 3d orbitals). (g) Free energy of AEM reaction pathway.

spectroscopy anlysis was performed to further probe the interfacial charge-transfer behavior (Figure S4). Compared with the control samples, V_2O_5@NiFe LDH/NF shows the smallest semicircle diameter, revealing its reduced charge-transfer resistance and improved electrode/electrolyte interfacial conductivity. In addition, the electrochemically active surface area analysis in Figure S5 indicates that V_2O_5@NiFe LDH/NF possesses a larger accessible active surface than pristine NiFe LDH/NF, which is beneficial for exposing more catalytic sites during OER. The linear sweep voltammetry (LSV) measured in different electrolytes (Figure S6) shows that V_2O_5@NiFe LDH/NF maintains comparable polarization behavior under various electrolyte environments, suggesting its favorable adaptability to alkaline seawater and tolerance toward Cl^--containing media. Temperature-dependent LSV measurements were further conducted to evaluate the reaction energy barrier (Figure S7). V_2O_5@NiFe LDH/NF consistently exhibits a higher current response and lower onset potential than NiFe LDH/NF across the tested temperature range, confirming its enhanced catalytic activity under varied thermal conditions. Based on the linear relationship between log(j) and T^{-1} at fixed potentials (Figure 2c), the apparent activation energy of V_2O_5@NiFe LDH/NF is calculated to be 31.68 kJ mol^{-1}, which is significantly lower than that of NiFe LDH/NF (41.39 kJ mol^{-1}), demonstrating that V_2O_5 incorporation effectively lowers the kinetic barrier of the OER process. Furthermore, the turnover frequency (TOF) analysis derived from electrochemical measurements (Figure 2d and S8) shows that V_2O_5@NiFe LDH/NF achieves a higher TOF at an η of 0.75 V, indicating that each accessible active site possesses enhanced intrinsic catalytic activity. As summarized in Figure 2e and Table S3, the catalytic performance of V_2O_5@NiFe LDH/NF compares favorably to most reported non-noble-metal-based electrocatalysts, highlighting its potential for alkaline seawater electrolysis.

DFT calculations were performed to gain deeper insight into the intrinsic electronic modulation induced by VO_4^{3-} modification (Figure 2f). Compared with pristine Fe-NiOOH-CO_3^{2-}, the VO_4^{3-}@Fe-NiOOH-CO_3^{2-} model exhibits a higher density of electronic states near the Fermi level, indicating enriched electronic states and improved charge-transport capability. This enhanced electronic structure is favorable for reducing interfacial charge-transfer resistance and accelerating OER kinetics. The d-band center analysis further reveals that the d-band center shifts upward from –1.74 eV for Fe-NiOOH-CO_3^{2-} to –1.69 eV after VO_4^{3-} modification, approaching the Fermi level. According to d-band center theory, such an upward shift can strengthen the orbital coupling between metal active sites and oxygenated intermediates, thereby optimizing the adsorption behavior of key OER intermediates, including *OH, *O, and *OOH, and facilitating reactant activation. To clarify the OER pathway,

pH-dependent electrochemical measurements were conducted. As shown in Figure S9, when the electrolyte pH increases from 12.5 to 14, V_2O_5@NiFe LDH/NF displays a more pronounced pH-dependent activity than NiFe LDH/NF, suggesting accelerated proton-coupled electron-transfer kinetics. Meanwhile, the nearly overlapped LSV curves obtained in different electrolytes (Figure S10) indicate that TMAOH has negligible influence on the electrode kinetics and oxygen evolution behavior. These results suggest that both catalysts mainly follow the adsorbate evolution mechanism (AEM) pathway. Isotope-labeled electrochemical mass spectrometry was further employed to identify the oxygen source during OER (Figure S11). Both samples show distinct m/z = 32 signals corresponding to continuously generated ^{16}O–^{16}O, whereas the m/z = 34 signal associated with ^{18}O–^{16}O remains close to the baseline throughout the measurement, excluding the substantial participation of lattice oxygen in O–O bond formation and oxygen release. Therefore, the AEM pathway was adopted for subsequent theoretical simulations based on the surface models shown in Figure S12. As displayed in Figure 2g, the elementary reaction free-energy profiles differ significantly between the two models. The maximum free-energy change of pristine Fe-NiOOH-CO_3^{2-} is 0.71 eV, whereas this value decreases sharply to 0.14 eV after VO_4^{3-} incorporation, indicating a substantially lowered reaction energy barrier and more favorable OER kinetics. These theoretical results are consistent with the electrochemical measurements and mechanistic analyses, demonstrating that VO_4^{3-} modification does not alter the inherent AEM pathway but effectively regulates the surface electronic structure and intermediate adsorption behavior, thereby enhancing the intrinsic catalytic activity of V_2O_5@NiFe LDH/NF.

Chronopotentiometric measurements were conducted to evaluate the operational durability of the catalysts under constant-current electrolysis (Figure 3a). The ion-exchange control experiment shows that carbonate-depleted V_2O_5@NiFe LDH-Cl/NF exhibits markedly weakened durability, confirming that interlayer CO_3^{2-} serves as an intrinsic inner shielding barrier against Cl^- attack (Figure S13). Compared with NiFe LDH/NF, V_2O_5@NiFe LDH/NF maintains a lower and more stable working potential throughout the test, indicating reduced energy consumption and superior long-term stability in alkaline seawater electrolyte (Table S4). To assess chlorine-related anodic side reactions, UV–vis spectroscopy was employed to detect ClO^- species generated during electrolysis. As shown in Figure 3b and S14, V_2O_5@NiFe LDH/NF exhibits only weak absorption responses with negligible spectral variation at different electrolysis times, suggesting that the modified electrode effectively suppresses Cl^- adsorption and improves OER selectivity, thereby inhibiting chlorine oxidation reactions in seawater. Consistently, the post-electrolysis XPS spectra in Figure 3c shows an almost negligible Cl 2p signal, further confirming that V_2O_5 modification markedly weakens Cl^- accumulation on the catalyst surface and reduces the probability of chlorine-mediated corrosion. In situ Raman spectroscopy was further performed to monitor the structural evolution of the catalysts under applied potentials (Figure 3d). For V_2O_5@NiFe LDH/NF, the oxidation of Ni^{2+} to Ni^{3+} and the reconstruction toward the active NiOOH phase occur at 1.3–1.4 V, indicating that the introduction of V_2O_5 lowers the oxidation barrier of Ni sites and promotes the generation of OER-active species at relatively low potentials. Meanwhile, the emergence of a band around 900 cm^{-1} can be assigned to V–O vibrations associated with reconstructed VO_4^{3-} species, evidencing the transformation of V_2O_5 into a vanadate-derived anionic protective layer during OER. The interfacial ion-distribution

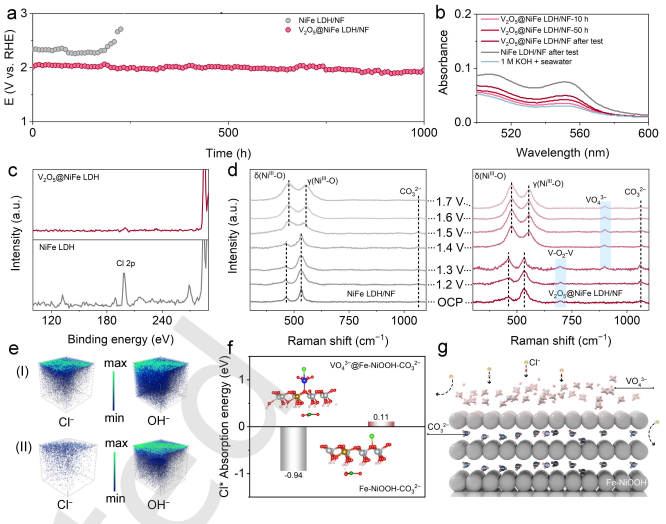

Figure 3 (a) Stability test of V_2O_5@NiFe LDH/NF and NiFe LDH/NF at 1000 mA cm^{-2} in 1 M KOH + seawater. (b) Ultraviolet-visible absorption spectra of the collected electrolytes from V_2O_5@NiFe LDH/NF and NiFe LDH/NF stability test at 1000 mA cm^{-2}. (c) XPS spectra in Cl 2p regions of V_2O_5@NiFe LDH and NiFe LDH after the stability test. (d) In-situ Raman data for catalysts during the OER process. (e) 3D TOF-SIMS images of catalysts after reaction. (I) NiFe LDH/NF; (II) V_2O_5@NiFe LDH/NF. (f) Calculation of Cl* adsorption energy on Fe-NiOOH-CO_3^{2-} and VO_4^{3-}@Fe-NiOOH-CO_3^{2-}. (g) Schematic diagram of chlorine corrosion resistance mechanism.

analysis in Figure 3e further reveals that Cl^- are more dispersed and less enriched near the V_2O_5@NiFe LDH/NF interface, whereas a high local concentration of OH^- is retained, demonstrating that the modified anionic interface can simultaneously repel Cl^- and facilitate preferential OH^- transport/adsorption for accelerated OER kinetics. The suppressed side reactions are further supported by Figure S15, where the Faradaic efficiency approaches nearly 100% during ASO process. In addition, the corrosion analysis in Figure S16 shows that V_2O_5@NiFe LDH/NF possesses a higher corrosion potential and lower corrosion current, confirming its enhanced resistance to chloride-induced corrosion and improved electrochemical stability. Moreover, the corrosion polarization tests in 1 M KOH and neutral natural seawater further demonstrate the superior anti-corrosion adaptability of the dual-anion-protected V_2O_5@NiFe LDH/NF compared with NiFe LDH/NF (Figure S17). Theoretical Cl* adsorption free-energy calculations in Figure 3f further reveal the intrinsic origin of the anti-chloride behavior. The positive Cl* adsorption free energy on VO_4^{3-}@Fe-NiOOH-CO_3^{2-} indicates thermodynamically unfavorable Cl^- adsorption, verifying that the reconstructed VO_4^{3-} species effectively inhibits chloride binding at the catalyst surface. The competitive adsorption free-energy calculations show that V_2O_5@NiFe LDH/NF preferentially stabilizes OH^- over Cl*, confirming that the dual-anion protection promotes OH^- adsorption while suppressing Cl^- adsorption on the catalyst surface (Figure S18). Based on these experimental and theoretical results, the protection mechanism illustrated in Figure 3g can be proposed: the surface VO_4^{3-} anionic

layer cooperates with interlayer CO_3^{2-} species to establish a dual-anion protective interface, which shields Cl^- attack, promotes preferential OH^- transport, and thereby enhances both OER selectivity and long-term durability in alkaline seawater. Post-stability XRD, SEM, and XPS characterizations after stability test show that V_2O_5@NiFe LDH/NF largely preserves its structural integrity, surface composition, and morphology, further confirming its excellent long-term stability (Figures S19–S21). Moreover, ICP-OES analysis of the electrolyte after long-term electrolysis reveals only negligible leaching of Ni, Fe, and V species, further confirming the excellent structural stability and durability of V_2O_5@NiFe LDH/NF (Table S5).

As shown in Figure 4a, an alkaline seawater electrolyzer was assembled using Pt/C/NF as the cathode and V_2O_5@NiFe LDH/NF as the anode. A Pt/C/NF||RuO_2/NF device was also constructed as a benchmark for comparison. The LSV curves in Figure 4b show that Pt/C/NF||V_2O_5@NiFe LDH/NF electrolyzer requires a lower cell voltage than the Pt/C/NF||RuO_2/NF counterpart at the same *j*, demonstrating the superior anodic oxygen-evolution activity of V_2O_5@NiFe LDH/NF and its advantage in reducing the overall energy input for seawater splitting. The practical durability of the assembled electrolyzers was further evaluated by long-term galvanostatic electrolysis. As shown in Figure 4c and Table S6, the Pt/C/NF||V_2O_5@NiFe LDH/NF system maintains a stable operating voltage with negligible fluctuation over 1000 h of continuous operation, whereas the Pt/C/NF||RuO_2/NF system exhibits an obvious voltage increase, indicating gradual performance degradation during prolonged electrolysis. The intermittent electrolysis test in Figure 4d further confirms the robust operational stability of the Pt/C/NF||V_2O_5@NiFe LDH/NF device under dynamic working conditions. These results indicate that V_2O_5@NiFe LDH/NF not only delivers excellent activity in half-cell measurements but also retains high stability and durability in a practical alkaline seawater electrolyzer, highlighting its potential for long-term H_2 production under device-level operating conditions.

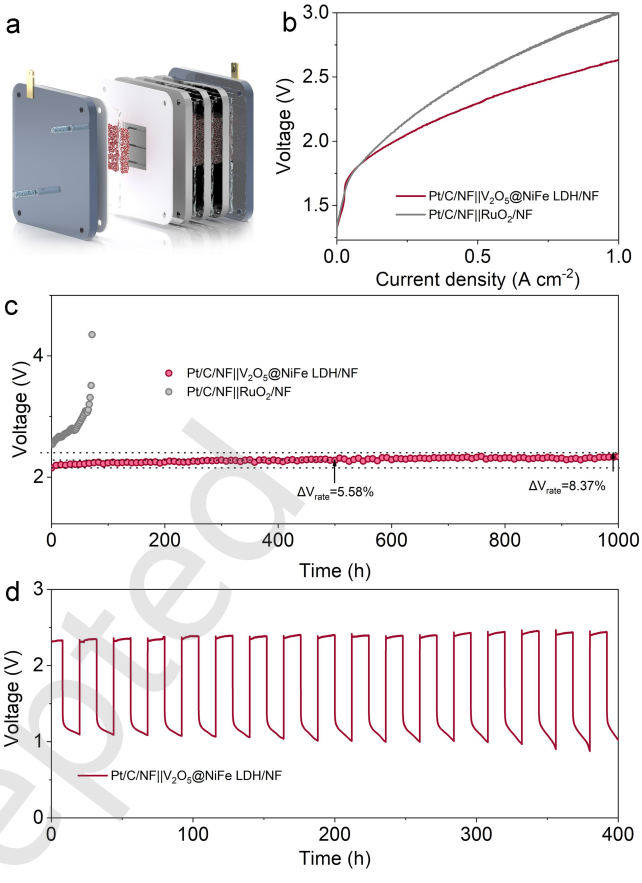

Figure 4 (a) Diagram of AEMWE. (b) Polarization curves. (c) Stability test of Pt/C/NF||V_2O_5@NiFe LDH/NF at a *j* of 400 mA cm^{-2} in 1 M KOH + seawater. (d) Stability test of Pt/C/NF||V_2O_5@NiFe LDH/NF at a *j* of 400 mA cm^{-2} in 1 M KOH + seawater.

4 Conclusions

In summary, a V_2O_5@NiFe LDH/NF composite catalyst was constructed and systematically investigated for ASO, with particular emphasis on its structural evolution, interfacial chemistry, and electrocatalytic behavior. Experimental results reveal that the surface V_2O_5 component undergoes in situ transformation into VO_4^{3-} species during electrolysis, which cooperates with interlayer CO_3^{2-} anions in NiFe LDH to establish a dynamically regulated anionic protection interface. Benefiting from this dual-anion modulation effect, the optimized V_2O_5@NiFe LDH/NF electrode exhibits excellent OER activity, requiring an η of only 370 mV to deliver 1000 mA cm^{-2}. It also maintains stable operation for 1000 h with negligible potential fluctuation, while achieving a Faradaic efficiency approaching 100% for OER, demonstrating remarkable durability and high reaction selectivity in alkaline seawater. When integrated into a membrane-electrode-assembly device, the catalyst enables a low cell voltage of 2.02 V at 500 mA cm^{-2} and sustains continuous operation for 1000 h. The proposed synergistic anion-modulation strategy effectively optimizes interfacial charge distribution, ion-transport behavior, and reaction selectivity, thereby balancing catalytic activity, structural robustness, and chlorine-corrosion resistance. This work provides a viable design principle for developing cost-effective and durable electrocatalysts for practical seawater electrolysis.

Acknowledgements

M. S. H. and A. F. extend their appreciation to the Deanship of Research and Graduate Studies at King Khalid University for funding this work through the Large Research Project under Grant number RGP2/29/46.

Electronic Supplementary Material: Supplementary material (SEM images, CV curves, LSV curves, UV-vis absorption spectra, XPS spectra, DEMS spectra, theoretical-calculation reaction pathway diagrams, and Tables S1–S6) is available in the online version of this article at https://doi.org/10.26599/NR.2026.94908974.

References

[1] Goldthau, A. The G20 must govern the shift to low-carbon energy. *Nature* **2017**, *546*, 203–205.

[2] Hydrogen as Emerging Fuel for De-Fossilizing Transport Sector; Valera, H.; Agarwal, A. K., Eds.; Springer Nature Singapore: Singapore, **2024**.

[3] Turner, J. A. Sustainable hydrogen production. *Science* **2004**, *305*, 972–974.

[4] Molecular Hydrogen in Health and Disease; Slezák, J.; Kura, B., Eds.; Springer Nature Switzerland: Cham, **2024**.

[5] Jiang, Z.; Ainiwaer, M.; Liu, J.; Ying, B.; Luo, F.; Sun, X. Hydrogen therapy: recent advances and emerging materials. *Biomater. Sci.* **2024**, *12*, 4136–4154.

[6] Lai, F.; Shang, H.; Jiao, Y.; Chen, X.; Zhang, T.; Liu, X. Recent progress and perspective on electrocatalysis in neutral media: Mechanisms, materials, and advanced characterizations. *Interdiscip. Mater.* **2024**, *3*, 492–529.

[7] Wang, Y.; Liu, Y.; Kim, M. G.; Qi, L.; Xue, Y.; Yang, W.; Liu, T.; Li, G.; Li, Y. Interfacial charge relay and dynamic electronic replenishment by a graphdiyne armor for stable RuO_2-based water electrolyser. *Nano Res.* **2026**, *19*, 94908680.

[8] Zhang, L.; Zhu, J.; Li, X.; Mu, S.; Verpoort, F.; Xue, J.; Kou, Z.; Wang, J. Nurturing the marriages of single atoms with atomic clusters and nanoparticles for better heterogeneous electrocatalysis. *Interdiscip. Mater.* **2022**, *1*, 51–87.

[9] Xu, X.; Chen, S.; Chen, P.; Guo, K.; Yu, X.; Tang, J.; Lu, W.; Miao, X. Cation vacancy modulated Cu_3P-CoP heterostructure electrocatalyst for boosting hydrogen evolution at high current densities and coupling Zn-H_2O battery. *J. Colloid Interface Sci.* **2024**, *674*, 624–633.

[10] Liang, J.; Li, J.; Dong, H.; Li, Z.; He, X.; Wang, Y.; Yao, Y.; Ren, Y.; Sun, S.; Luo, Y. et al. Aqueous alternating electrolysis prolongs electrode lifespans under harsh operation conditions. *Nat. Commun.* **2024**, *15*, 6208.

[11] Luo, M.; Sang, W.; Tian, Y.; Li, X.; Chen, J.; Fu, G.; Xia, Z.; Chen, C.; Xu, X.; Bu, T.; Peng, J.; Wang, J.; Kou, Z. 3D-printing starfish‐inspired gas‐evolving electrode scaffolds enable smpere‐level alkaline water electrolysis. *Adv. Mater.* **2026**, *38*, e73344.

[12] Jiang, B.; Zhu, J.; Xia, Z.; Lyu, J.; Li, X.; Zheng, L.; Chen, C.; Chaemchuen, S.; Bu, T.; Verpoort, F.; Mu, S.; Wu, J.; Wang, J.; Kou, Z. Correlating single-atomic ruthenium interdistance with long‐range interaction boosts hydrogen evolution reaction kinetics. *Adv. Mater.* **2023**, *36*, 2310699.

[13] Wang, J.; Cui, W.; Liu, Q.; Xing, Z.; Asiri, A. M.; Sun, X. Recent progress in cobalt-based heterogeneous catalysts for electrochemical water splitting. *Adv. Mater.* **2016**, *28*, 215–230.

[14] Xu, X.; Guo, K.; Sun, J.; Yu, X.; Miao, X.; Lu, W.; Jiao, L. Interface Engineering of Mo‐doped Ni_2P/Fe_xP-V multiheterostructure for efficient dual‐pH hydrogen evolution and overall water splitting. *Adv. Funct. Mater.* **2024**, *34*, 2400397.

[15] Postel, S. L. Entering an era of water scarcity: the challenges ahead. *Ecol. Appl.* **2000**, *10*, 941–948.

[16] Greve, P.; Kahil, T.; Mochizuki, J.; Schinko, T.; Satoh, Y.; Burek, P.; Fischer, G.; Tramberend, S.; Burtscher, R.; Langan, S. et al. Global assessment of water challenges under uncertainty in water scarcity projections. *Nat. Sustain.* **2018**, *1*, 486–494.

[17] Wu, Q.; Gao, Q.; Zhang, C.; Wang, J.; Li, J.; Yang, F.; Sun, S.; Hamdy, M. S.; Farouk, A.; Sun, X. Emerging electrocatalysts and electrolyzers for high-current-density direct seawater electrolysis. *Green Chem.* **2026**, *28*, 7552–7585.

[18] Wang, H.; Li, D.; Liu, M.; Kong, Y.; Yang, C.; Li, Z.; Sun, S.; Wang, S.; Hamdy, M. S.; Farouk, A. et al. Sodium alginate-modified NiFe layered double hydroxide for robust alkaline seawater oxidation at high current densities. *Chin. Chem. Lett.* **2026**, DOI: 10.1016/j.cclet.2026.112945.

[19] Fan, R.; Liu, C.; Li, Z.; Huang, H.; Feng, J.; Li, Z.; Zou, Z. Ultrastable electrocatalytic seawater splitting at ampere-level current density. *Nat. Sustain.* **2024**, *7*, 158–167.

[20] Ni, T.; Zhao, W.; Zhang, S.; Zaki, M. E. A.; Toghan, A.; Huang, M. Ion-sieve-mediated continuous lattice oxygen regeneration for stable seawater electrolysis. *Nano Res.* **2026**, *19*, 94908681.

[21] Liu, J.; Duan, S.; Shi, H.; Wang, T.; Yang, X.; Huang, Y.; Wu, G.; Li, Q. Rationally designing efficient electrocatalysts for direct seawater splitting: challenges, achievements, and promises. *Angew. Chem. Int. Ed.* **2022**, *61*, e202210753.

[22] Dresp, S.; Dionigi, F.; Klingenhof, M.; Strasser, P. Direct electrolytic splitting of seawater: opportunities and challenges. *ACS Energy Lett.* **2019**, *4*, 933–942.

[23] Yu, L.; Ning, M.; Wang, Y.; Yuan, C.; Ren, Z. Direct seawater electrolysis for hydrogen production. *Nat. Rev. Mater.* **2025**, *10*, 857–873.

[24] Zuo, W.; Liu, M.; Sun, S.; Yang, Y.; Li, Z.; Zhang, X.; Yang, C.; Wang, H.; Shakir, I.; Liu, X. et al. Synergistic chloride resistance via hydrogen-bond network dynamic optimization and electrostatic repulsion for alkaline seawater oxidation. *Chin. J. Catal.* **2026**, *87*, 295–304.

[25] Tong, W.; Forster, M.; Dionigi, F.; Dresp, S.; Sadeghi Erami, R.; Strasser, P.; Cowan, A. J.; Farràs, P. Electrolysis of low-grade and saline surface water. *Nat. Energy* **2020**, *5*, 367–377.

[26] He, X.; Li, Z.; Yao, Y.; Luo, F.; Sun, X.; Tang, B. Surface and interfacial engineering of electrocatalysts for seawater electrolysis. *Acc. Chem. Res.* **2026**, *59*, 518–528.

[27] Ren, Y.; Wang, D.; Sun, S.; Li, Z.; Yao, Y.; Yang, Z.; Wang, H.; Song, J.; Yang, C.; Cai, Z. et al. Dual-function surface engineering for enhancing anode stability in alkaline seawater oxidation. *Nat. Commun.* **2026**, *17*, 5178.

[28] Pan, D.; Zhai, T.; Zhang, R.; Yuan, Y.; Wang, H.; Lu, S. Advancing layered double hydroxides (LDHs) as the anodes for efficient anion-exchange-membrane water electrolyzers. *Nano Res.* **2026**, *19*, 94907937.

[29] Zhou, D.; Li, P.; Lin, X.; McKinley, A.; Kuang, Y.; Liu, W.; Lin, W.; Sun, X.; Duan, X. Layered double hydroxide-based electrocatalysts for the oxygen evolution reaction: identification and tailoring of active Sites, and superaerophobic nanoarray electrode assembly. *Chem. Soc. Rev.* **2021**, *50*, 8790−8817.

[30] Liu, Y.; Hu, H.; Wang, K.; Huang, J.; Wang, D. Advancing seawater electrolysis: NiFe-LDH-based electrocatalysts for the oxygen evolution reaction. *Adv. Energy Mater.* **2026**, *16*, e04101.

[31] Sun, X.; Shen, W.; Liu, H.; Xi, P.; Jaroniec, M.; Zheng, Y.; Qiao, S.-Z. Corrosion-resistant NiFe anode towards kilowatt-scale alkaline seawater electrolysis. *Nat. Commun.* **2024**, *15*, 10351.

[32] Wu, Y.; Sun, S.; Li, T.; Yang, C.; Cai, Z.; Li, Z.; Ren, Y.; Zheng, D.; Luo, Y.; Ibrahim, F. A. et al. Pb-doped NiFe layered double hydroxide for efficient and durable seawater oxidation at high current densities. *Nano Res.* **2025**, *18*, 94907656.

[33] Cai, Z.; Liang, J.; Li, Z.; Yan, T.; Yang, C.; Sun, S.; Yue, M.; Liu, X.; Xie, T.; Wang, Y. et al. Stabilizing NiFe sites by high-dispersity of nanosized and anionic Cr species toward durable seawater oxidation. *Nat. Commun.* **2024**, *15*, 6624.

[34] Ding, P.; Song, H.; Chang, J.; Lu, S. N-doped carbon dots coupled NiFe-LDH hybrids for robust electrocatalytic alkaline water and seawater oxidation. *Nano Res.* **2022**, *15*, 7063–7070.

[35] Wang, T.; Wei, X.; Cheng, Z.; Li, X.; Liu, K.; Ming, L.; Zhang, L.; Lyu, J.; Pan, K.; Li, Z. et al. In situ constructed chromate cover stabilizes seawater oxidation via competitively repelling chloride ions. *Nano Res.* **2025**, *18*, 94907952.

[36] Liang, J.; Cai, Z.; Li, Z.; Geng, M.; Wang, H.; Wang, Z.; Li, T.; Wu, T.; Luo, F.; Sun, X. et al. Expanded negative electrostatic network-assisted seawater oxidation and high-salinity seawater reutilization. *ACS Nano*

2025, *19*, 1530–1546.

[37] Henry, H. K.; Johnston, B.; Liau, D.; Sahadeo, E.; Lee, S. B. Dual effect of structure and hydration on magnesium-ion insertion into electrodeposited V_2O_5 thin films. *J. Electrochem. Soc.* **2020**, 167, 110523.

[38] Zhao, Z.; Zhang, S.; Su, Z.; Lin, S.; Qu, W. Construction of Fe,V-codoped Ni_3S_2/V_2O_5 toward highly efficient large current density freshwater/seawater splitting. *Langmuir* **2026**, *42*, 1317–1328.

[39] Mendialdua, J.; Casanova, R.; Barbaux, Y. XPS studies of V_2O_5, V_6O_{13}, VO_2 and V_2O_3. *J. Electron Spectrosc. Relat. Phenom.* **1995**, *71*, 249–261.

[40] Wang, H.; Li, Z.; Hong, S.; Yang, C.; Liang, J.; Dong, K.; Zhang, H.; Wang, X.; Zhang, M.; Sun, S. et al. Tungstate intercalated NiFe layered double hydroxide enables long-term alkaline seawater oxidation. *Small* **2024**, *20*, 2311431.

Electronic Supplementary Material

Dual-anion synergistic protection of NiFe layered double hydroxide for durable alkaline seawater oxidation

Zhengwei Cai[1§], Zixiao Li[2§], Yang Li[3§], Wencong Xu[2], Mingyu Liu[2], Dongrui Li[2], Shengjun Sun[2], Mohamed S. Hamdy[4], Asmaa Farouk[4], Xiaodong Zhang[1](✉), Qiang Yu[1](✉), and Xuping Sun[2,5](✉)

[1] *Laoshan Laboratory, Qingdao 266237, China*

[2] *College of Chemistry, Chemical Engineering and Materials Science, Shandong Normal University, Jinan 250014, China*

[3] *Division of Gastrointestinal Surgery Ward, Department of Generl Surgery, West China Hospital, Sichuan University, Chengdu 610041, China*

[4] *Central Labs & Research Center for Advanced Materials Science (RCAMS), King Khalid University, Abha 61413, Saudi Arabia*

[5] *Center for High Altitude Medicine, West China Hospital, Sichuan University, Chengdu 610041, China*

[§] Zhengwei Cai, Zixiao Li, and Li Yang contributed equally to this work

Supporting information to https://doi.org/10.26599/NR.2026.94908974

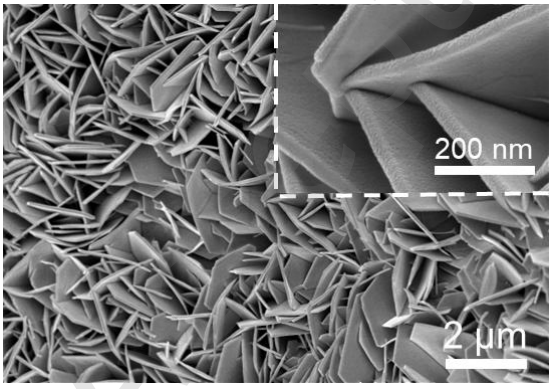

Figure S1. Low- and high (inset)-magnification SEM images of NiFe LDH/NF.

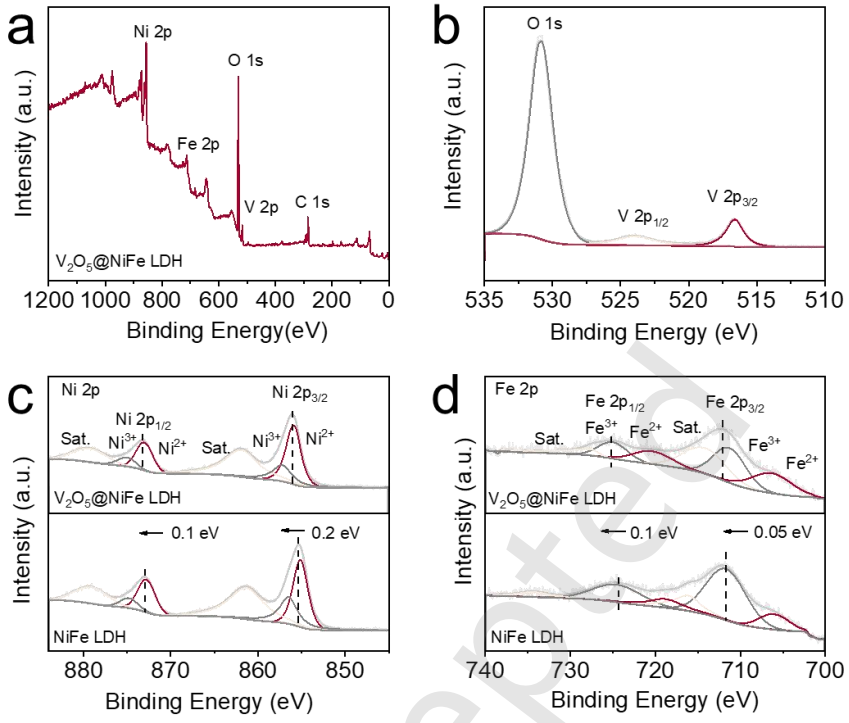

Figure S2. (a) Survey spectra of XPS for V_2O_5@NiFe LDH. High-resolution XPS spectra of V_2O_5@NiFe LDH and NiFe LDH in the (b) V 2p, (c) Ni 2p, and (d) Fe 2p.

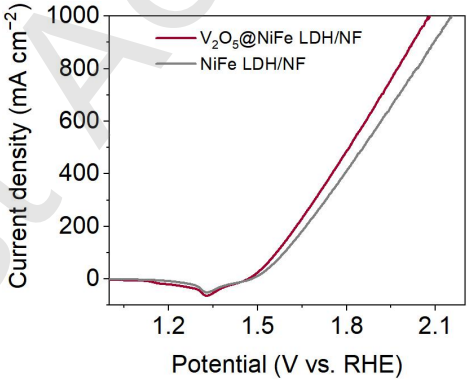

Figure S3. LSV curves without iR compensation.

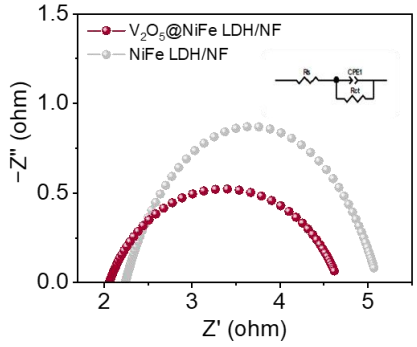

Figure S4. Nyquist plots of V_2O_5@NiFe LDH/NF and NiFe LDH/NF in 1 M KOH + seawater.

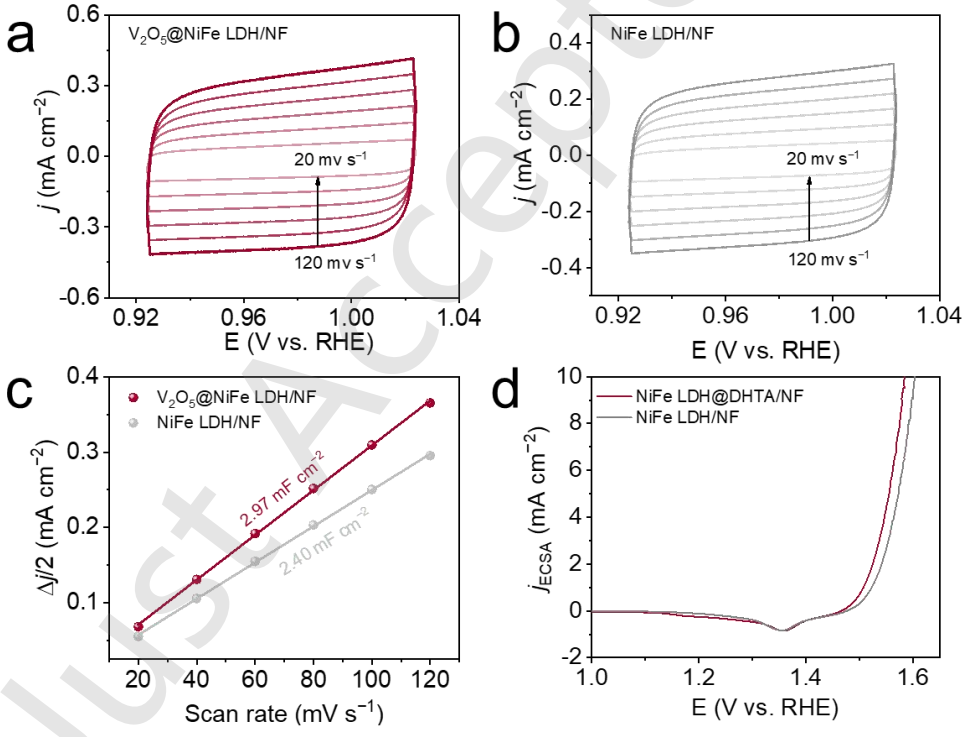

Figure S5. CV curves of (a) V_2O_5@NiFe LDH/NF and (b) NiFe LDH/NF in the non-Faraday region at various scan rates in 1 M KOH + seawater. (c) Comparison of C_{dl} values for V_2O_5@NiFe LDH/NF and NiFe LDH/NF electrodes.

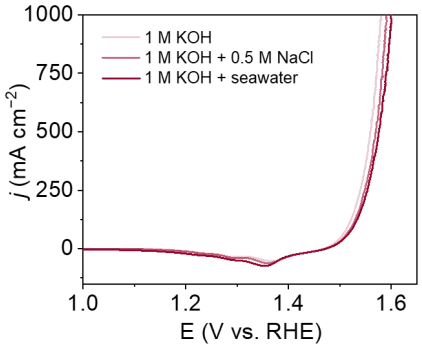

Figure S6. LSV curves of V_2O_5@NiFe LDH/NF in different electrolytes.

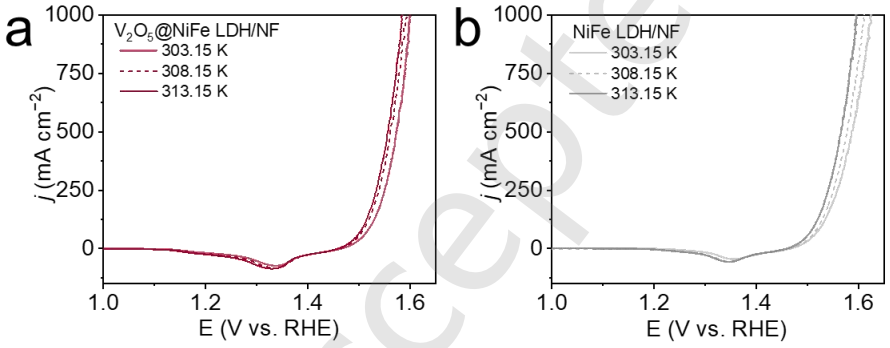

Figure S7. LSV curves of (a) V_2O_5@NiFe LDH/NF and (b) NiFe LDH/NF toward OER at different temperatures.

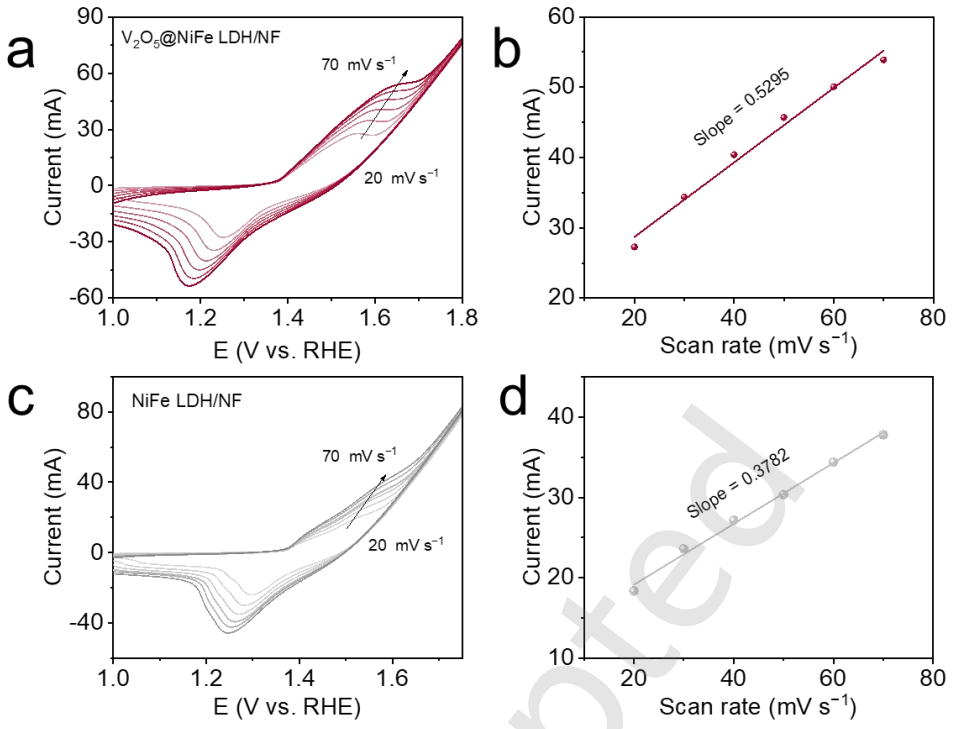

Figure S8. CV curves for (a) V_2O_5@NiFe LDH/NF and (c) NiFe LDH/NF at different scan rates increasing from 20 to 70 mV s^{-1} in 1 M KOH + seawater. Oxidation peak current versus scan rate plots for (b) V_2O_5@NiFe LDH/NF and (d) NiFe LDH/NF.

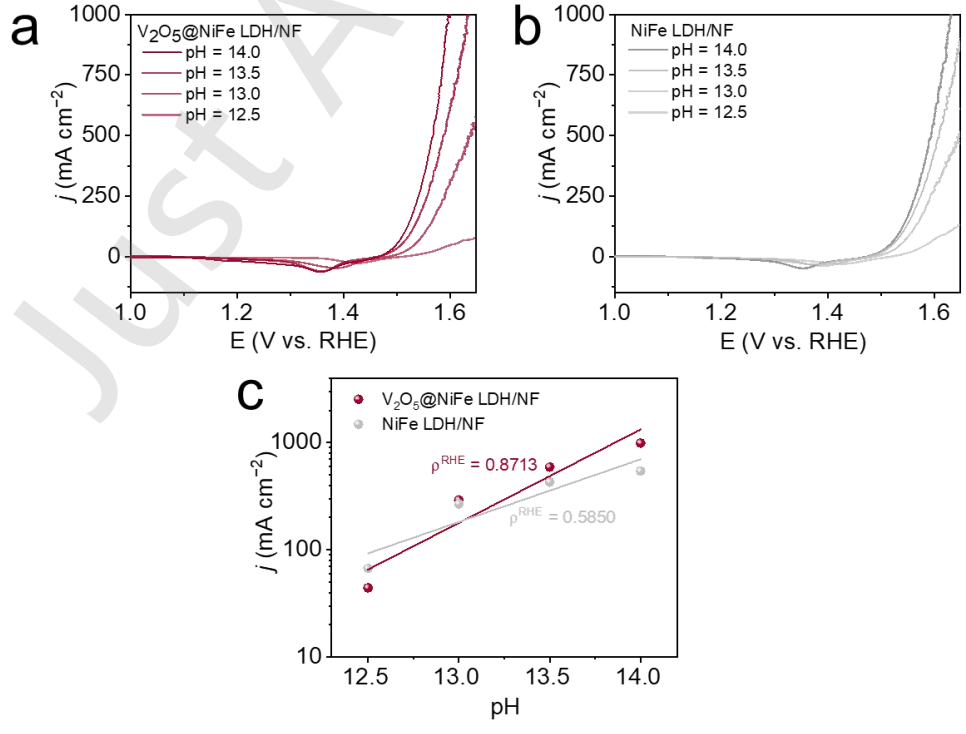

Figure S9. *j*-E curves of activated V_2O_5@NiFe LDH/NF and NiFe LDH/NF in alkaline seawater with different pH values and the logarithms of *j* at 1.60 V vs. RHE against the pH.

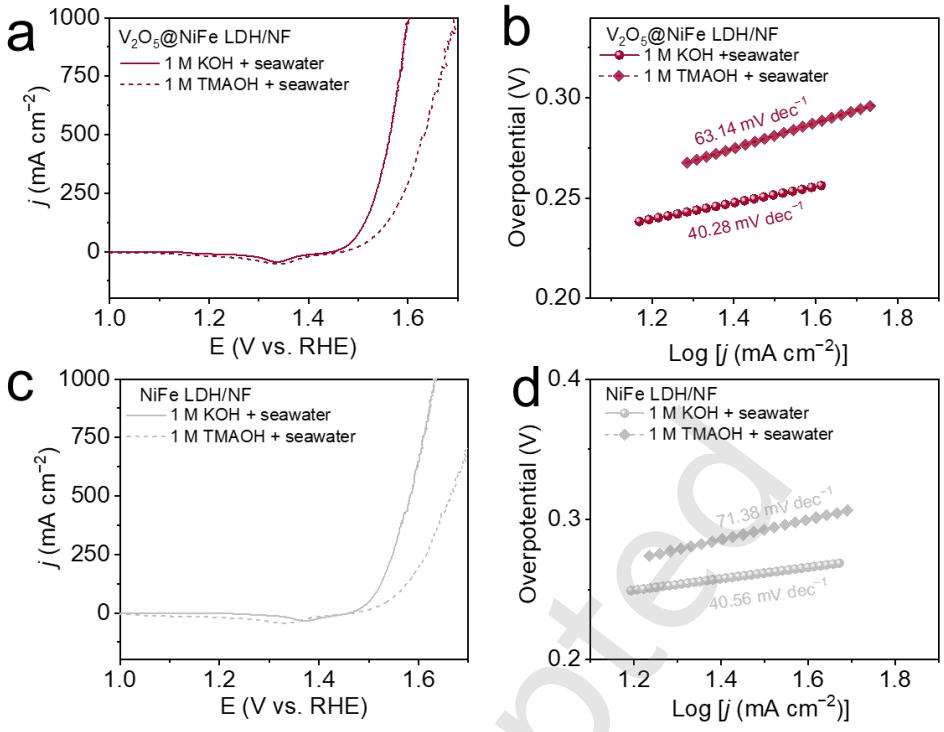

Figure S10. Comparison of LSV curves and derived Tafel slopes of NiFe LDH/NF and V_2O_5@NiFe LDH/NF in 1 M KOH + seawater and 1 M TMAOH + seawater.

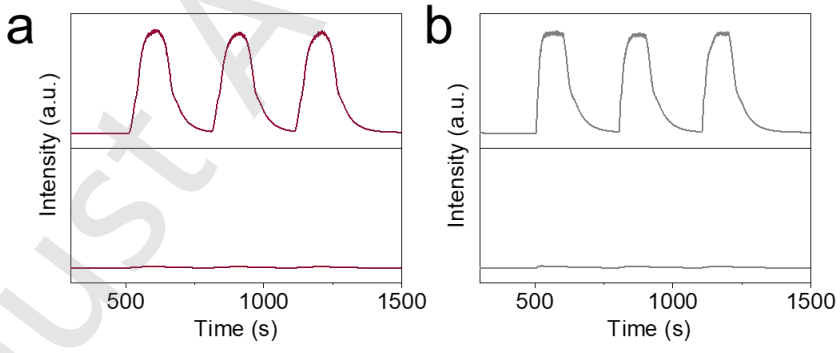

Figure S11. Current-time curves and corresponding DEMS signals recorded on activated (a) V_2O_5@NiFe LDH/NF and (b) NiFe LDH/NF in 1 M KOH + seawater.

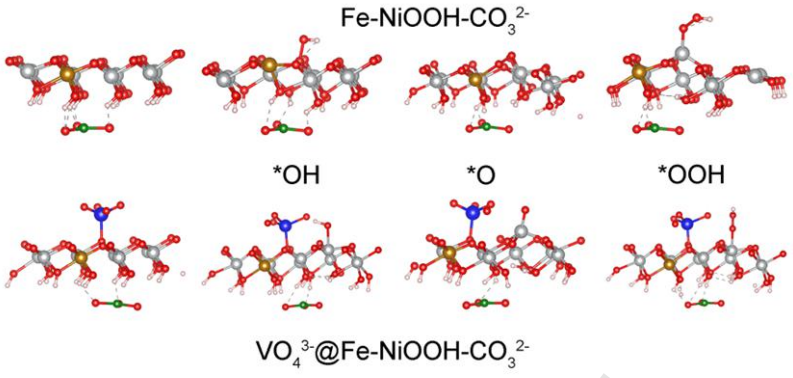

Figure S12. The reaction pathway diagram of the AEM mechanism.

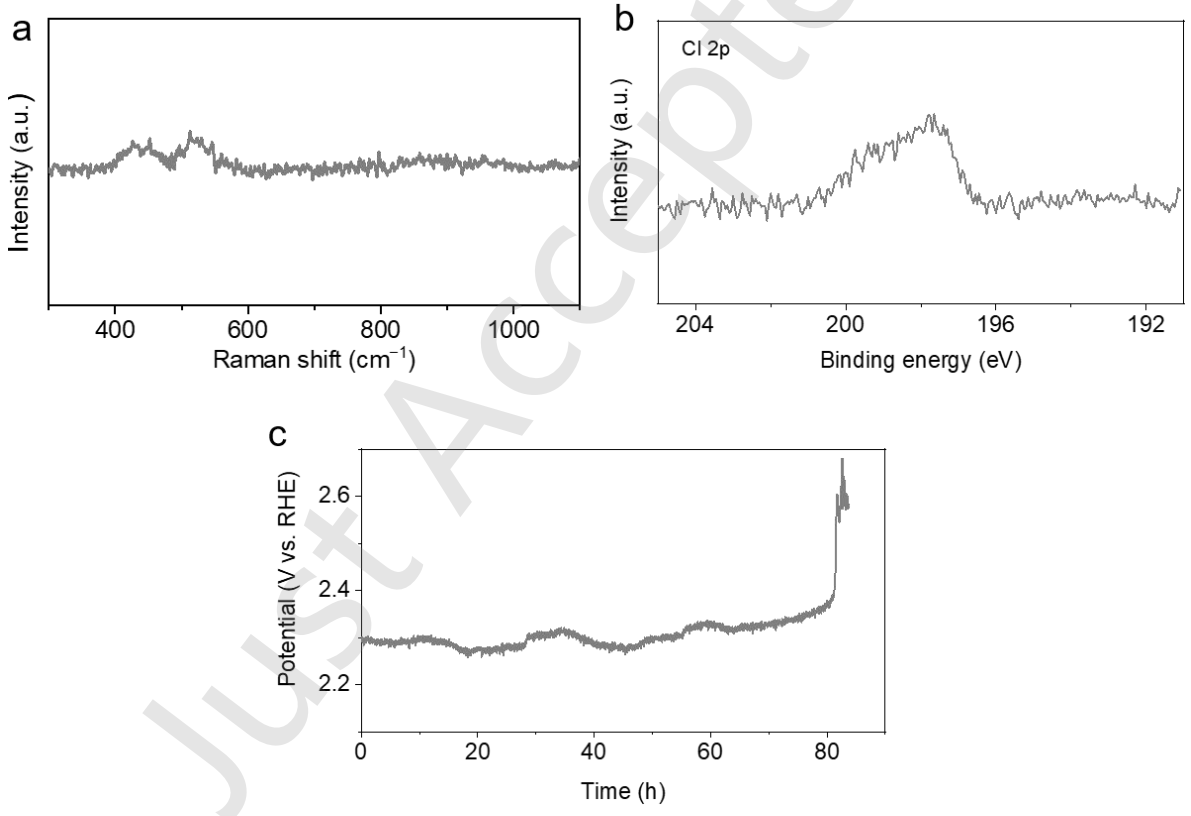

Figure S13. Control experiment for verifying the intrinsic protection role of interlayer CO_3^{2-}. (a) Raman spectrum of NiFe LDH/NF after NaCl immersion, (b) Cl 2p XPS spectrum of NaCl-treated NiFe LDH, and (c) chronopotentiometric curve of V_2O_5@NiFe LDH-Cl at 1000 mA cm^{-2} in alkaline seawater.

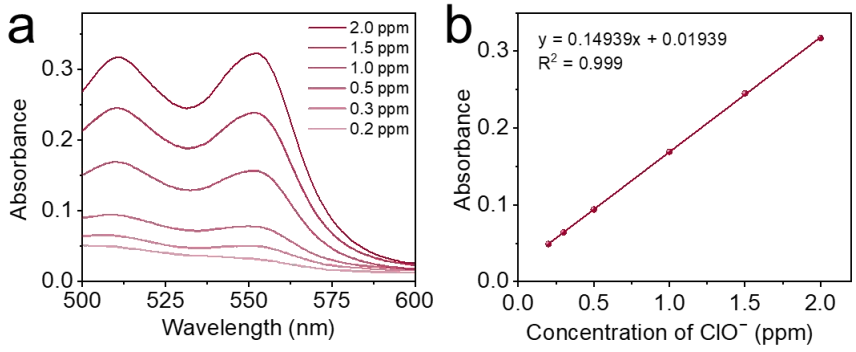

Figure S14. (a) UV-vis absorption spectra of various active chlorine concentrations and (b) corresponding linear fit.

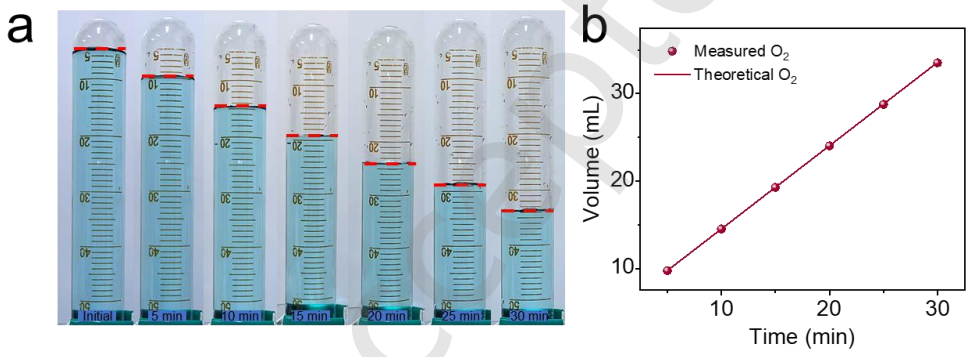

Figure S15. (a) Collection of oxygen evolved from seawater oxidation at a *j* of 1 A cm^{-2} by water drainage method. (b) Comparison between the amount of collected and theoretical O_2 for V_2O_5@NiFe LDH/NF at a *j* of 1 A cm^{-2} in 1 M KOH + seawater.

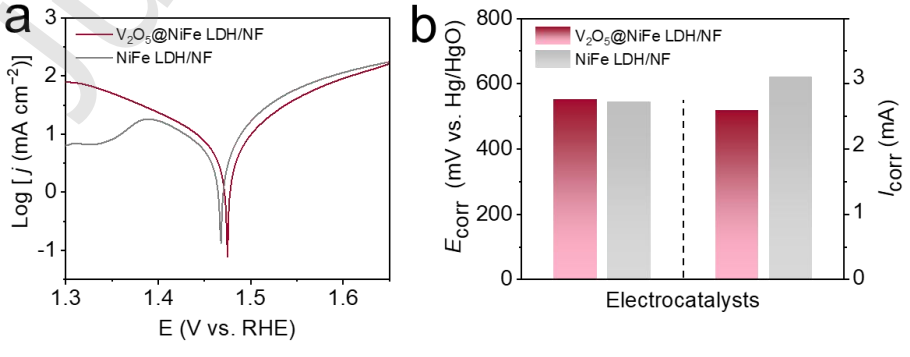

Figure S16. (a) Corrosion polarization curves and (b) corresponding corrosion potentials and corrosion *j* of V_2O_5@NiFe LDH/NF and NiFe LDH/NF in 1 M KOH + seawater.

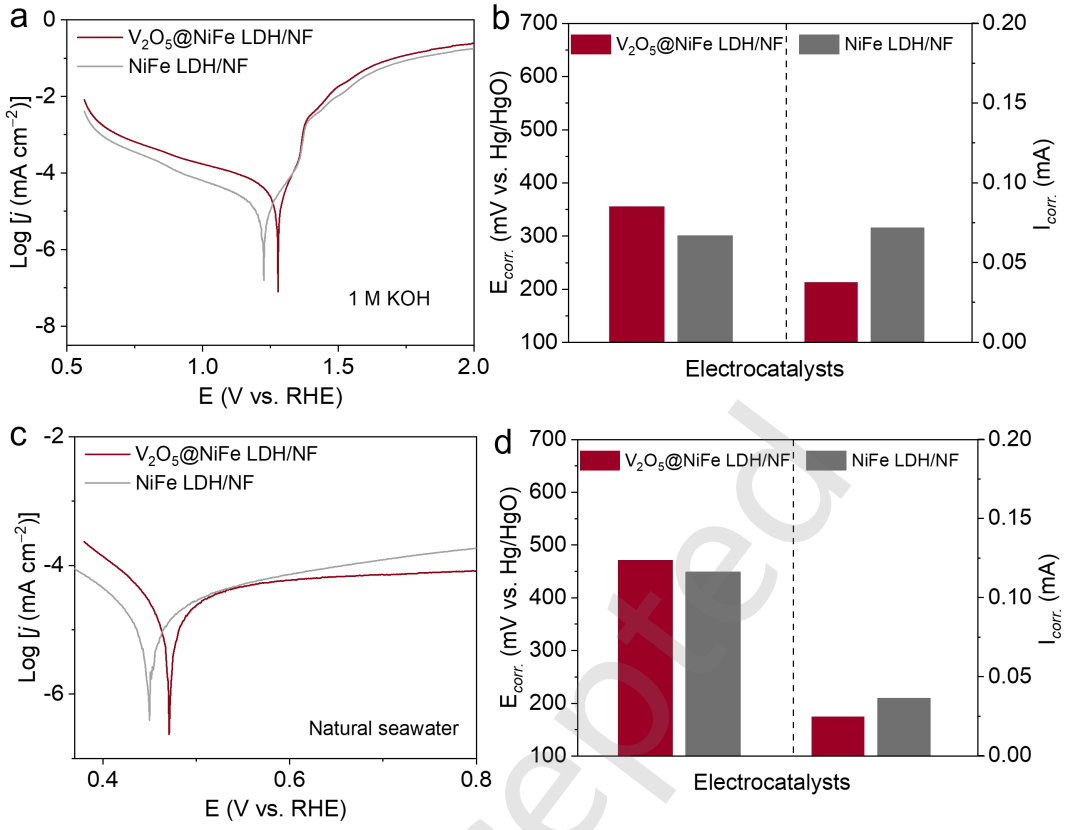

Figure S17. Corrosion polarization tests of V_2O_5@NiFe LDH/NF and NiFe LDH/NF. (a, b) Polarization curves and corresponding potential values in 1 M KOH. (c, d) Polarization curves and corresponding potential values in natural seawater.

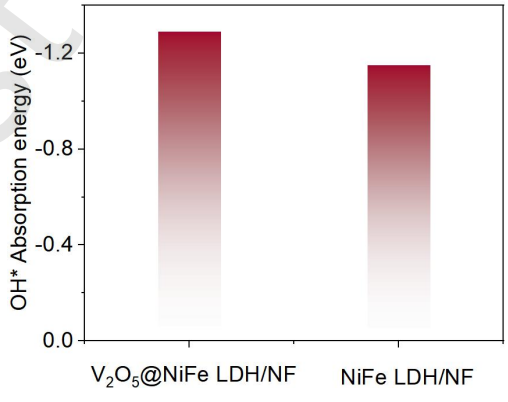

Figure S18. Calculation of Cl* adsorption energy on Fe-NiOOH-CO_3^{2-} and VO_4^{3-}@Fe-NiOOH-CO_3^{2-}.

Figure S19. SEM image of V_2O_5@NiFe LDH/N seawater.

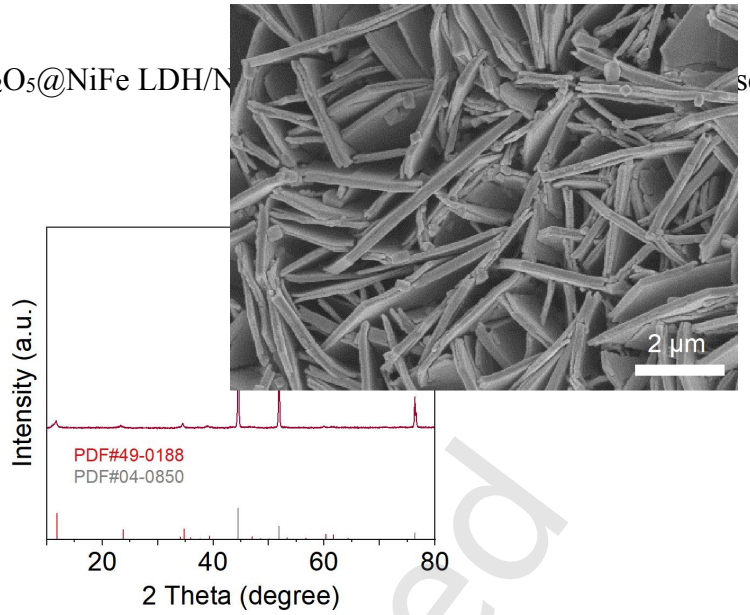

Figure S20. XRD pattern of V_2O_5@NiFe LDH/NF after the stability test in 1 M KOH + seawater.

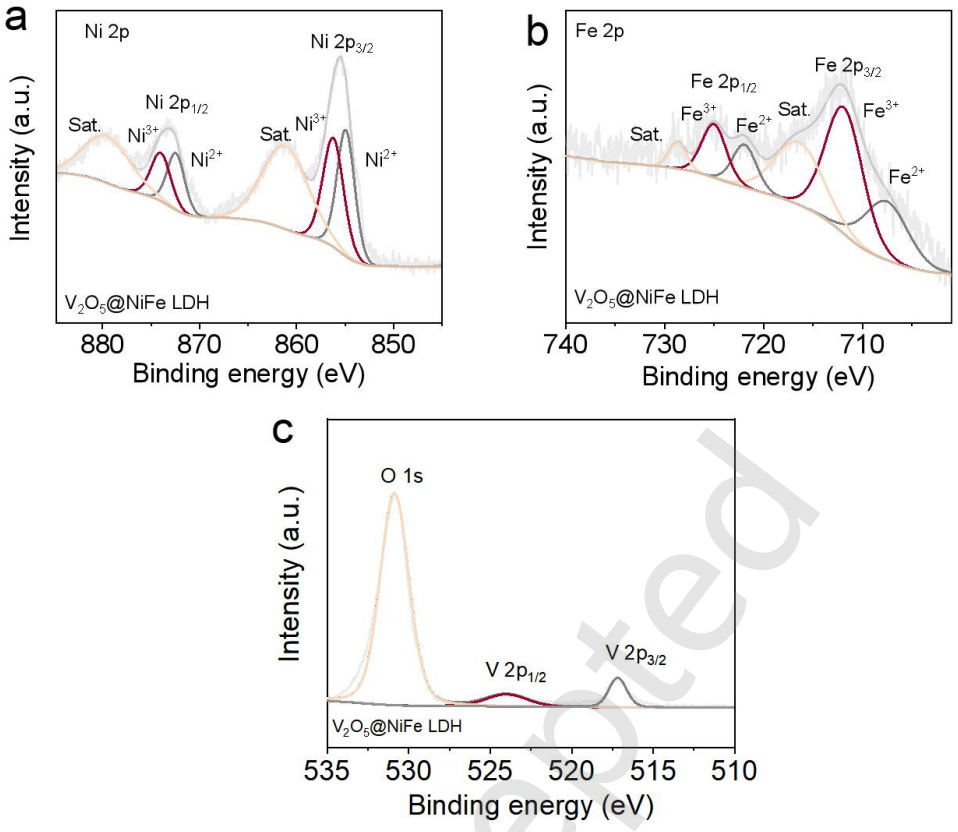

Figure S21. XPS spectra of V_2O_5@NiFe LDH in the (a) Ni 2p, (b) Fe 2p, and (c) V 2p regions after the stability test.

Table S1. V content in V_2O_5@NiFe LDH/NF determined by ICP-OES after three separate electrodeposition procedures.

Experiment number	Content (mg cm^{-2})
1	0.37
2	0.38
3	0.37

Table S2. Ion compositions of the natural seawater (before the seawater alkalization) and alkaline seawater (after the seawater alkalization) used in this work.

Species	Conc. [mg L^{-1}] for natural seawater	Conc. [mg L^{-1}] for alkaline seawater
Mg^{2+}	975.86	0.67
Ca^{2+}	532.09	7.35
K^{+}	439.73	34133.89
Na^{+}	9682.31	10498.12
SO_4^{2-}	655.79	658.13

Notes: The seawater was collected from Huangdao district, Qingdao city, China. The pH value for natural seawater was around 7.95, and the pH for alkaline seawater was around 13.98.

Table S3. Comparison of overpotentials at 1000 mA cm^{-2} for V_2O_5@NiFe LDH/NF with reported electrocatalysts in alkaline seawater.

Catalysts	Electrolyte	Current Density (mA cm^{-2})	Overpotential (mV)	Ref.
V_2O_5@NiFe LDH/NF	**1 M KOH + seawater**	**1000**	**370**	**This work**
SiF_6^{2-}-NiFe LDH/NF	1 M KOH + seawater	1000	371	*Catal. Sci. Technol.* **2025**, *15*, 4386−4391
Pb-NiFe LDH/NF	1 M KOH + seawater	1000	381	Nano Res. **2025**, 18, 94907656
NiFe LDH-CeW@NFF	1 M KOH + seawater	1000	387	*Appl. Catal. B Environ. Energy* **2023**, *330*, 122612
Ce-NiFe LDH/NF	1 M KOH + seawater	1000	390	*J. Energy Chem.* 2024, *91*, 306–312
NiFe LDH@PP/NF	1 M KOH + seawater	1000	390	*J. Mater. Chem. A* **2025**, *13*, 25329–25334
NiFe-MOF@Ni_2P/$Ni(OH)_2$/NF	1 M KOH + seawater	1000	394	*J. Colloid Interface Sci.* **2023**, *643*, 17–25
NiMoN@NiFeN	1 M KOH + seawater	1000	398	*Nat. Commun.* **2019**, *10*, 5106
NiFeO-CeO_2/NF	1 M KOH + seawater	1000	408	*ACS Nano* **2023**, *17*, 16008−16019
TS-NiFe LDH/NF	1 M KOH + seawater	1000	412	*Small* **2024**, *20*, 2311431
Fe-NiS/NF	1 M KOH + seawater	1000	420	*Inorg. Chem.* **2023**, *62*, 7976−7981
Ni_2P-Fe_2P/NF	1 M KOH + seawater	1000	431	*Adv. Funct. Mater.* **2021**, *31*, 2006484
S-Ni/Fe(OOH)/NF	1 M KOH + seawater	1000	462	*Energy Environ. Sci.* **2020**, *13*, 3439–3446
RuNi-Fe_2O_3	1 M KOH + seawater	1000	497	*Chin. J. Catal.* **2022**, *43*, 2202–2211

Table S4. Comparison of the stability at different current density for V_2O_5@NiFe LDH/NF with previously reported electrocatalysts in alkaline seawater.

Catalysts	Electrolyte	Current Density (mA cm^{-2})	Time (h)	Ref.
V_2O_5@NiFe LDH/NF	**1 M KOH + seawater**	**1000**	**1000**	**This work**
Ce-NiFe LDH/NF	1 M KOH + seawater	1000	500	*J. Energy Chem.* **2024**, *91*, 306–312
NiFe LDH-CeW@NFF	1 M KOH + seawater	1000	100	*Appl. Catal. B Environ. Energy* **2023**, *330*, 122612
NiFe-MOF@Ni_2P/$Ni(OH)_2$/NF	1 M KOH + seawater	500	120	*J. Colloid Interface Sci.* **2023**, *643*, 17–25
NiFeO-CeO_2/NF	1 M KOH + seawater	1000	200	*ACS Nano* **2023**, *17*, 16008−16019
TS-NiFe LDH/NF	1 M KOH + seawater	1000	350	*Small* **2024**, *20*, 2311431
Fe-NiS/NF	1 M KOH + seawater	500	25	*Inorg. Chem.* **2023**, *62*, 7976−7981
NiFe LDH@PCM/NF	1 M KOH + seawater	1000	500	*Small* **2025**, *21*, 2408642
NiPOx@NiFe LDH/NF	1 M KOH + seawater	1000	600	*J. Colloid Interface Sci.* **2025**, *687*, 708–714
NiCoP foam	1 M KOH + seawater	1000	300	*J. Mater. Chem. A* **2024**, *12*, 2680–2684
NiMoSx@NiFe-LDH/NF	1 M KOH + seawater	500	500	Inorg. Chem. Front. **2023**, 10, 2766–2775
(NiFe)C_2O_4/NF	1 M KOH + seawater	1000	600	*Angew. Chem. Int. Ed.* **2024**, *63*, e202316522
Ni_3S_2/Fe-NiP_x/NF	1 M KOH + seawater	1000	35	*Adv. Sci.* **2022**, *9*, 2104846
MnCo/NiSe/NF	1 M KOH + seawater	500	200	*Appl. Catal. B Environ. Energy* **2023**, *325*, 122355
NiFe LDH@PTPA/NF	1 M KOH + seawater	1000	600	*ACS Mater. Lett.* **2024**, *6*, 5248–5255
BZ-NiFe-LDH/CC	1 M KOH + seawater	500	100	*Nano Res. Energy* **2022**, *1*, 9120028
B-Co_2Fe LDH/NF	1 M KOH + seawater	500	100	*Nano Energy* **2021**, *83*, 105838
Fe_2P/Ni_3N/NF	1 M KOH + seawater	500	40	*Small* **2023**, *19*, 2207082
CDs-Mn-Co_xP/NF	1 M KOH + seawater	500	100	*Small* **2024**, *20*, 2402478
La-$Ni(OH)_2$/NF	1 M KOH + seawater	500	500	*Catal. Sci. Technol.* **2024**, *14*, 2717–2721
Ni_3FeN@C/NF	1 M KOH + seawater	500	100	*J. Mater. Chem. A* **2021**, *9*, 13562–13569

$P_{4.8}$-NiFe ANs-400/NF	1 M KOH + seawater	100	100	*Appl. Catal. B Environ. Energy* **2024**, *342*, 123376
$Fe_2P/Ni_{1.5}Co_{1.5}N/Ni_2P$	1 M KOH + seawater	100	40	*ACS Nano* **2023**, *17*, 1681–1692
Mn-FeP_v@IF	1 M KOH + seawater	100	45	*Small* **2024**, *20*, 2308613
F/Fe-CoP_v@IF	1 M KOH + seawater	100	20	*Appl. Catal. B Environ. Energy* **2023**, *328*, 122487

Table S5. Element analysis of V_2O_5@NiFe LDH/NF before and after stability test by ICP-OES.

	Element	Content (mg cm^{-2})
before stability test	Ni	1.51
	Fe	1.46
	V	0.37
after stability test	Ni	1.39
	Fe	1.28
	V	0.31

Table S6. Comparison of the cell tolerance at different current densities for V_2O_5@NiFe LDH/NF with previously reported electrocatalysts in alkaline seawater.

Catalysts	Electrolyte	Current Density (mA cm^{-2})	Time (h)	Ref.
Pt/C/NF||V_2O_5@NiFe LDH/NF	**1 M KOH + seawater**	**500**	**1000**	**This work**
Pt/C/NF|| Ce-NiFe LDH/NF	1 M KOH + seawater	300	120	*J. Energy Chem.* **2024**, *91*, 306–312
Ni_2P-Fe_2P/NF|| Ni_2P-Fe_2P/NF	1 M KOH + seawater	100	70	*Adv. Funct. Mater.* **2021**, *31*, 2006484
Ni_3N@C/NF|| Ni_3FeN@C/NF	1 M KOH + seawater	100	100	*J. Mater. Chem. A* **2021**, *9*, 13562–13569
F-FeCoP_v@IF|| F-FeCoP_v@IF	1 M KOH + seawater	120	100	*Appl. Catal. B Environ. Energy* **2023**, *328*, 122487
Pt/C/NF||NiNH@NiFe LDH/NF	1 M KOH + seawater	500	460	*Inorg. Chem.* **2025**, *64*, 23108–23114
Fe-doped Ni_2P||Fe-doped Ni_2P	1 M KOH + seawater	500	100	*Inorg. Chem.* **2017**, *56*, 1041–1044
CoFeOF/NF|| CoFeOF/NF	1 M KOH + seawater	400	140	*Chem. Eng. J.* **2024**, *480*, 146545
FeMo-NiP_x/NF|| FeMo-NiP_x/NF	1 M KOH + seawater	400	200	*Inorg. Chem. Front.* **2024**, *11*, 498–507
NiPS/NF||NiPS/NF	1 M KOH + seawater	200	60	*J. Energy Chem.* **2022**, *75*, 66–73
NiCoHPi@Ni_3N/NF||Ni CoHPi@Ni_3N/NF	1 M KOH + seawater	200	40	*ACS Appl. Mater. Interfaces* **2022**, *14*, 22061–22070
Co-Fe_2P/NF|| Co-Fe_2P/NF	1 M KOH + seawater	100	24	*Appl. Catal. B Environ. Energy* **2021**, *297*, 120386